Supporting Information:

Separating Bulk and Surface Processes in NiO_x Electrocatalysts for Water Oxidation

Sacha Corby[~1], Miguel-García Tecedor[~2], Sven Tengeler[3], Céline Steinert[3], Benjamin Moss[1], Camilo A. Mesa[1], Hany F. Heiba[4], Anna A. Wilson[1], Bernhard Kaiser[3], Wolfram Jaegermann[3]*, Laia Francàs[1]*, Sixto Gimenez[2]*, James R. Durrant[1]*

[1]Department of Chemistry and the Centre for Plastic Electronics, Imperial College London, South Kensington, London, SW7 2AZ, UK
[2]Insitute of Advanced Materials (INAM), University Jaume I, 12071 Castello de la Plana, Spain
[3]Institute of Material Science, Technical University Darmstadt, 64287 Darmstadt, Germany
[4]Earth Science and Engineering, Imperial College London, South Kensington, London, SW7 2AZ, UK

~*These authors contributed equally to this work*

**Corresponding: j.durrant@imperial.ac.uk, laia.francas@uab.cat, sjulia@fca.uji.es, jaegermann@surface.tu-darmstadt.de*

Contents

A – Synthesis of NiO_x films

The NiO_x films were deposited via magnetron sputtering onto FTO glass at room temperature and with a power setting of 15 W and a base pressure ≤ 10^{-7} mbar. The deposition was performed in a 0.03 mbar argon/oxygen atmosphere (19.6 sccm Ar and 0.4 sccm O_2) employing a 99.99% pure Ni target obtained from Kurt J. Lesker. Before starting each deposition, the target was sputtered at 100 W with the shutter closed in order to remove possible contaminants. The nickel layer thickness was determined from the changes in XPS core level intensities, as discussed in a previous publication.[1] The samples were rotated during deposition to ensure homogeneous growth.

B – Morphological, Compositional and Electrochemical Measurements

Morphological and compositional characterization of the electrodes was studied by Field Emission Scanning Electron Microscopy (SEM) with a JSM-7000F JEOL FEG-SEM system (Tokyo, Japan) equipped with an INCA 400 Oxford EDS analyzer (Oxford, U.K.) operating at 15 kV.

X-ray photo-electron spectroscopy (XPS) was carried out using a Thermo K-Alpha spectrometer with monochromated Al Kα radiation. Survey scans were collected over the 0−1400 eV binding energy range with 1 eV resolution and a pass energy of 200 eV. Higher resolution scans (0.1 eV) encompassing the principal peaks of C (1s), O (1s), and N (2p) were also collected at a pass energy of 50 eV. Peaks were modelled using CasaXPS. Peak positions were calibrated to adventitious carbon (284.5 eV).

The Raman measurements were performed with a WITec Apyron confocal microscope using a 532 nm laser with a power of 40 mW, a grating of 1800 lines/mm, a spectrometer of 300 mm and an optical objective Zeiss EC Epiplan-Neofluar Dic 100x/0.9.

The photoelectrochemical characterization of the electrodes was carried out by means of cyclic and linear voltammetry in the dark in a 0.1 M KOH solution of pH 13 (standard reaction grade). The electrochemical cell was composed by the working electrode, an Ag/AgCl (3 M KCl) reference electrode and a Pt wire as a counter electrode. All the potentials were referred to the Reversible Hydrogen Electrode (RHE) through the Nernst equation: $V_{RHE} = V_{Ag/AgCl} + V^0_{Ag/AgCl} + 0.059 \cdot pH$, where $V^0_{Ag/AgCl}(3M\ KCl) = 0.21\,V$. All the experiments were carried out by using an AutoLab potentiostat PGSTAT302. Electrochemical Impedance Spectroscopy (EIS) measurements were performed between 0.1 Hz and 1 MHz with 20 mV of amplitude perturbation, with a step potential of 50 mV in the anodic direction. The EIS data were analyzed with ZView software (Scribner associates), fitting the raw data to an equivalent circuit model (see Figure S8) for extracting both capacitances and resistances. With the extracted capacitance values from EIS; Mott-Schottky analysis was carried out using the expression:

$\frac{1}{C_{SC}^2} = \frac{2}{\varepsilon_0 \varepsilon_r e N_D A^2}\left(\phi_{SC} - \frac{kT}{e}\right)$, where $\phi_{SC} = V - V_{FB}$

C_{SC} represents space charge capacitance, e is the elementary charge, ε_0 is the permittivity in vacuum, ε_r is the relative permittivity of NiO_x, (taken as 9.1),[2] N_D is the donor density (can be exchanged for acceptor density, N_A), A is the area, k is the Boltzmann constant and T is the absolute temperature, taken as 298 K. From this analysis, the values of the flat-band potential (V_{FB}) and the acceptor density (N_A) were extracted. The depletion layer width was calculated to validate the employed model through the equation:

$w = \sqrt{\frac{2\varepsilon_0 \varepsilon_r}{e N_D}\left(\phi_{SC} - \frac{kT}{e}\right)}$

C – SEM and EDS

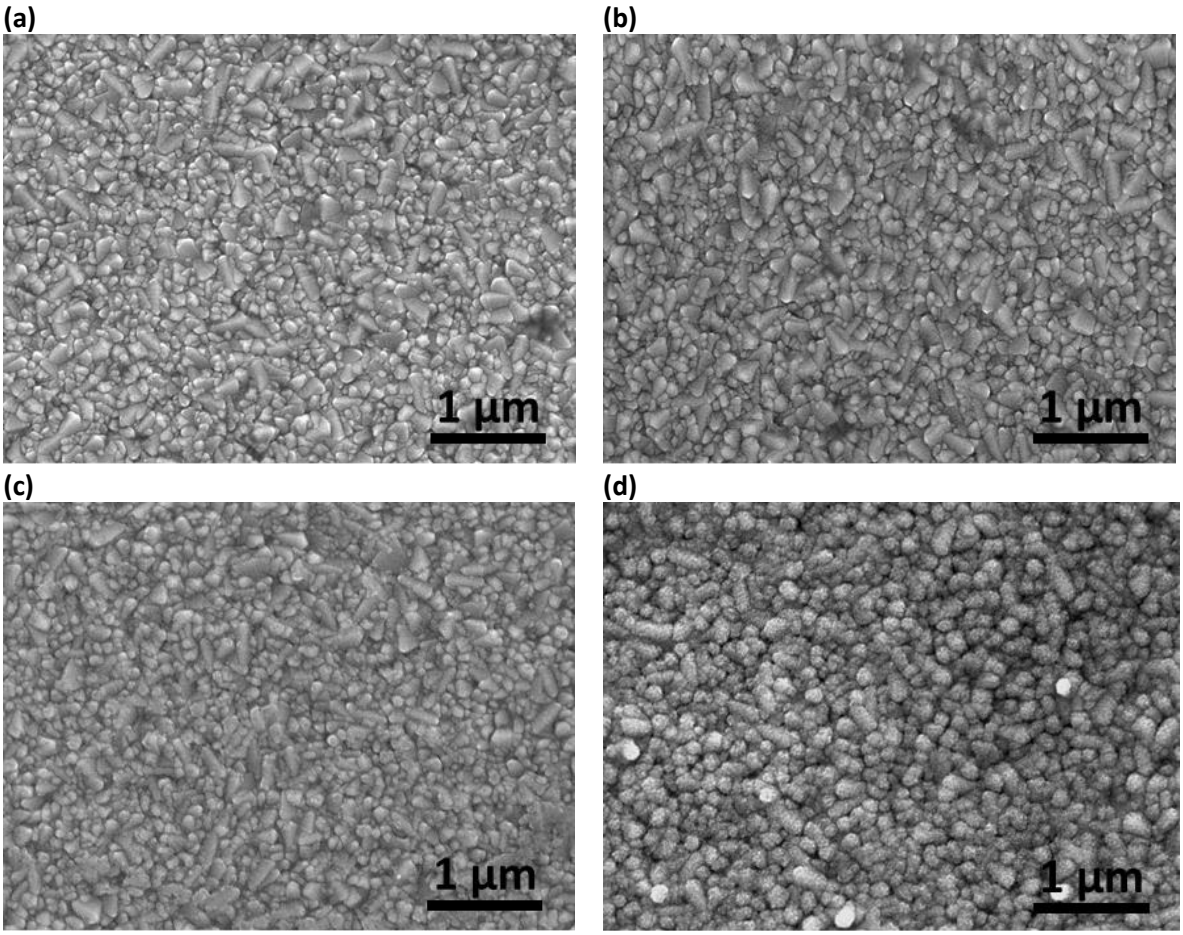

Figure S1. Top view SEM images of (a) 5 nm, (b) 10 nm, (c) 20 nm and (d) 100 nm as-synthesised NiO_x films (before electrochemical activation).

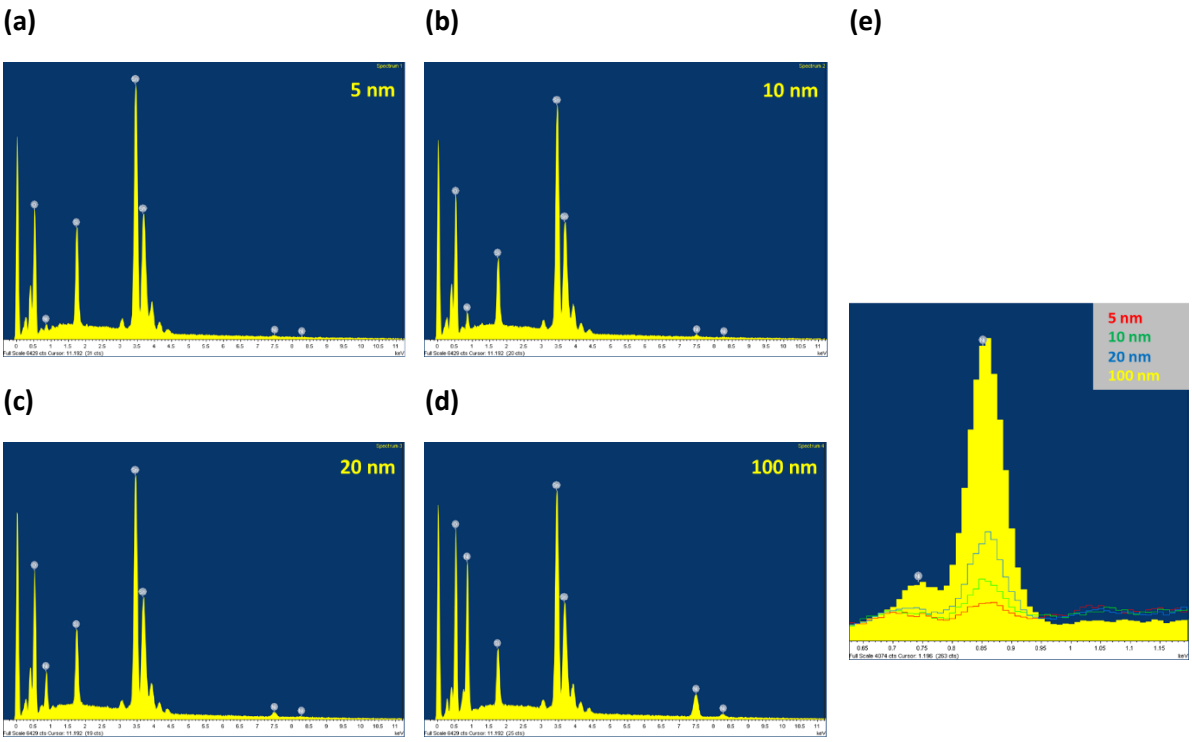

Figure S2. EDS spectra of (a) 5 nm, (b) 10 nm, (c) 20 nm, (d) 100 nm samples. (e) Comparison of the Ni L_α line for the different samples.

As the Ni content observed by EDS will be proportional to the amount of NiO_x deposited, it is evident from the relative intensities of the Ni L_α lines, overlaid in panel (e), that the thicknesses of the samples are approximately 5, 10, 20 and 100 nm, as reported.

D - XRD

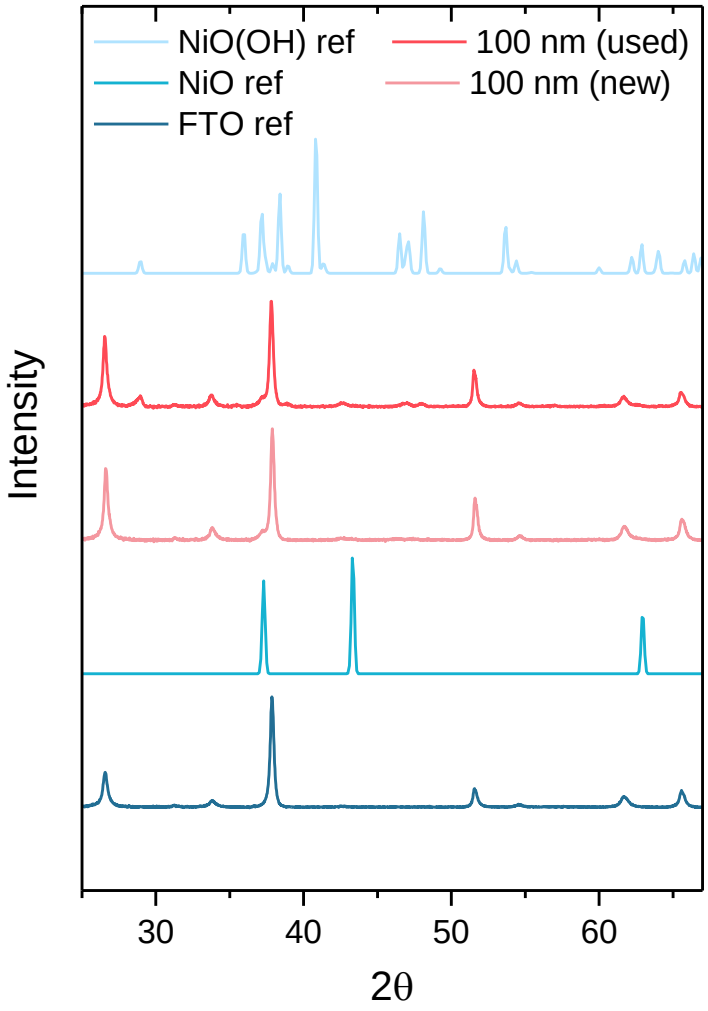

Figure S3. XRD characterisation of 100 nm NiO_x films, before (pink) and after (red) electrochemical activation in 0.1 M KOH. References for FTO, NiO (bunsenite) and NiO(OH) are given in blue. There are small differences in the NiOx film following activation, with new peaks corresponding to NiOOH present. However, the bulk of the film, after drying for 1 day, can be expected to be largely similar to the bunsenite shown before use. The 5, 10 and 20 nm films were below the resolution limit for the experiment.

E - XPS

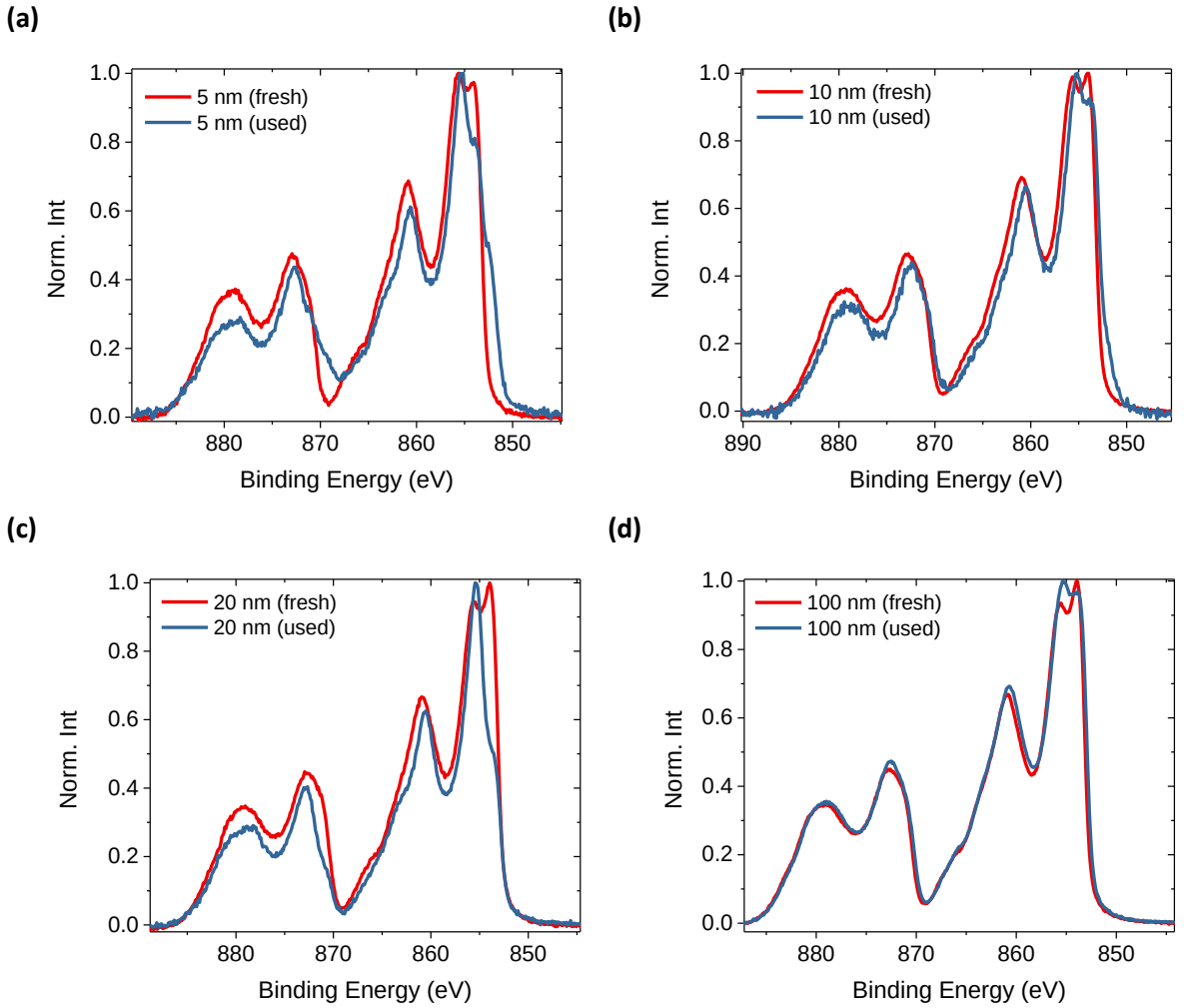

Figure S4. XPS characterisation of the Ni 2p 3/2 and 1/2 peaks for each film thickness (a) 5 nm, (b) 10 nm, (c) 20 nm, (d) 100 nm, before (fresh, red) and after (used, blue) electrochemical activation in 0.1 M KOH. Small changes in the peak shapes can be observed after usage, most notable in the thinner films and becoming less striking with thickness. We tentatively assign these peak shifts to the long-lasting oxidation of some Ni centres in the film, as NiO_x is converted to NiOOH by activation.

(a)

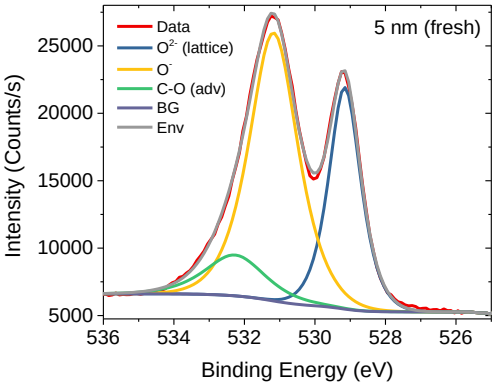
Data
O2- (lattice)
O-
C-O (adv)
BG
Env
5 nm (fresh)
Intensity (Counts/s)
Binding Energy (eV)

(b)

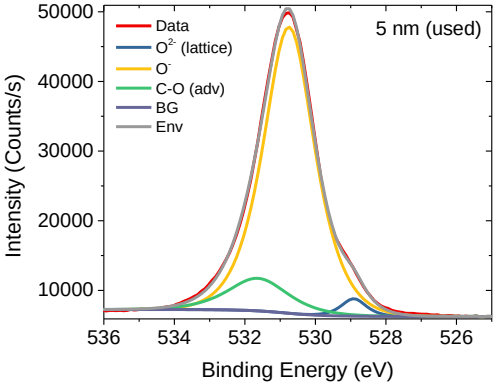
Data
O2- (lattice)
O-
C-O (adv)
BG
Env
5 nm (used)
Intensity (Counts/s)
Binding Energy (eV)

(c)

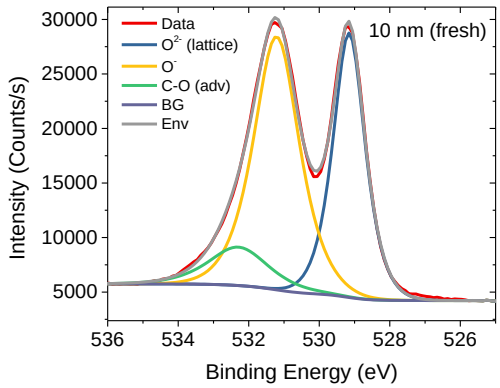
Data
O2- (lattice)
O-
C-O (adv)
BG
Env
10 nm (fresh)
Intensity (Counts/s)
Binding Energy (eV)

(d)

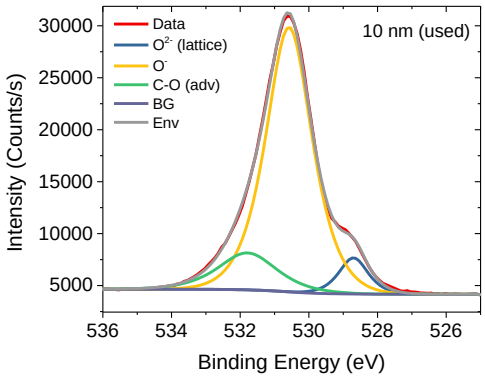
Data
O2- (lattice)
O-
C-O (adv)
BG
Env
10 nm (used)
Intensity (Counts/s)
Binding Energy (eV)

(e)

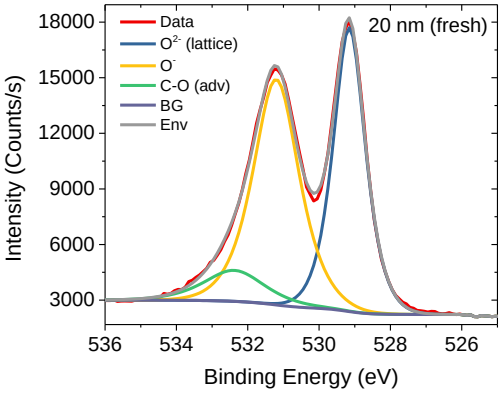
Data
O2- (lattice)
O-
C-O (adv)
BG
Env
20 nm (fresh)
Intensity (Counts/s)
Binding Energy (eV)

(f)

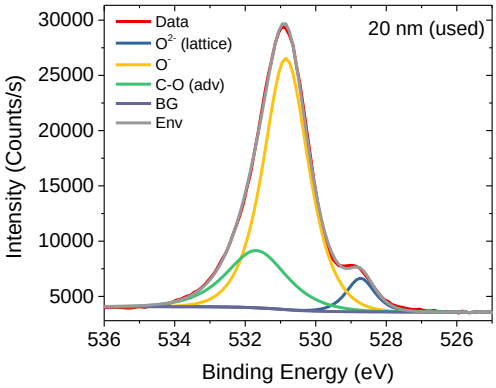
Data
O2- (lattice)
O-
C-O (adv)
BG
Env
20 nm (used)
Intensity (Counts/s)
Binding Energy (eV)

(g)

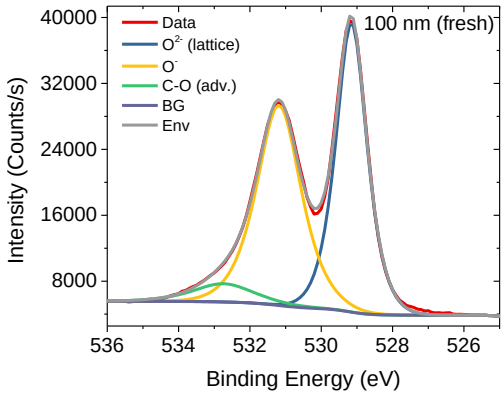
Data
O2- (lattice)
O-
C-O (adv.)
BG
Env
100 nm (fresh)
Intensity (Counts/s)
Binding Energy (eV)

(h)

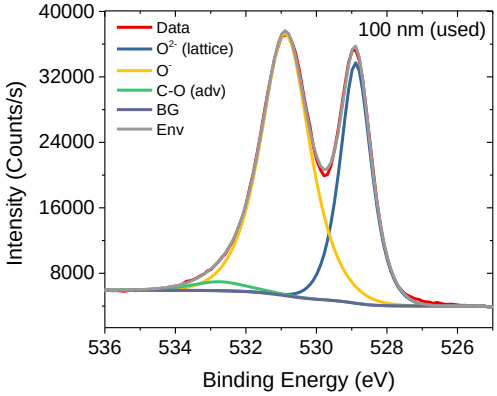
Data
O2- (lattice)
O-
C-O (adv)
BG
Env
100 nm (used)
Intensity (Counts/s)
Binding Energy (eV)

Figure S5. XPS characterisation on the O 1s peak before use for each film thickness (a) 5 nm, (c) 10 nm, (e) 20 nm, (g) 100 nm, and after use (b) 5 nm, (d) 10 nm, (f) 20 nm, (h) 100 nm. The reduction of the peak at 529 eV after use is most prevalent in the thinner films, in line with the greater oxidation of Ni (Figure S3) (i.e. oxidation of NiO_x and $Ni(OH)_2$ to NiOOH).

F – Electrochemical Impedance Spectroscopy

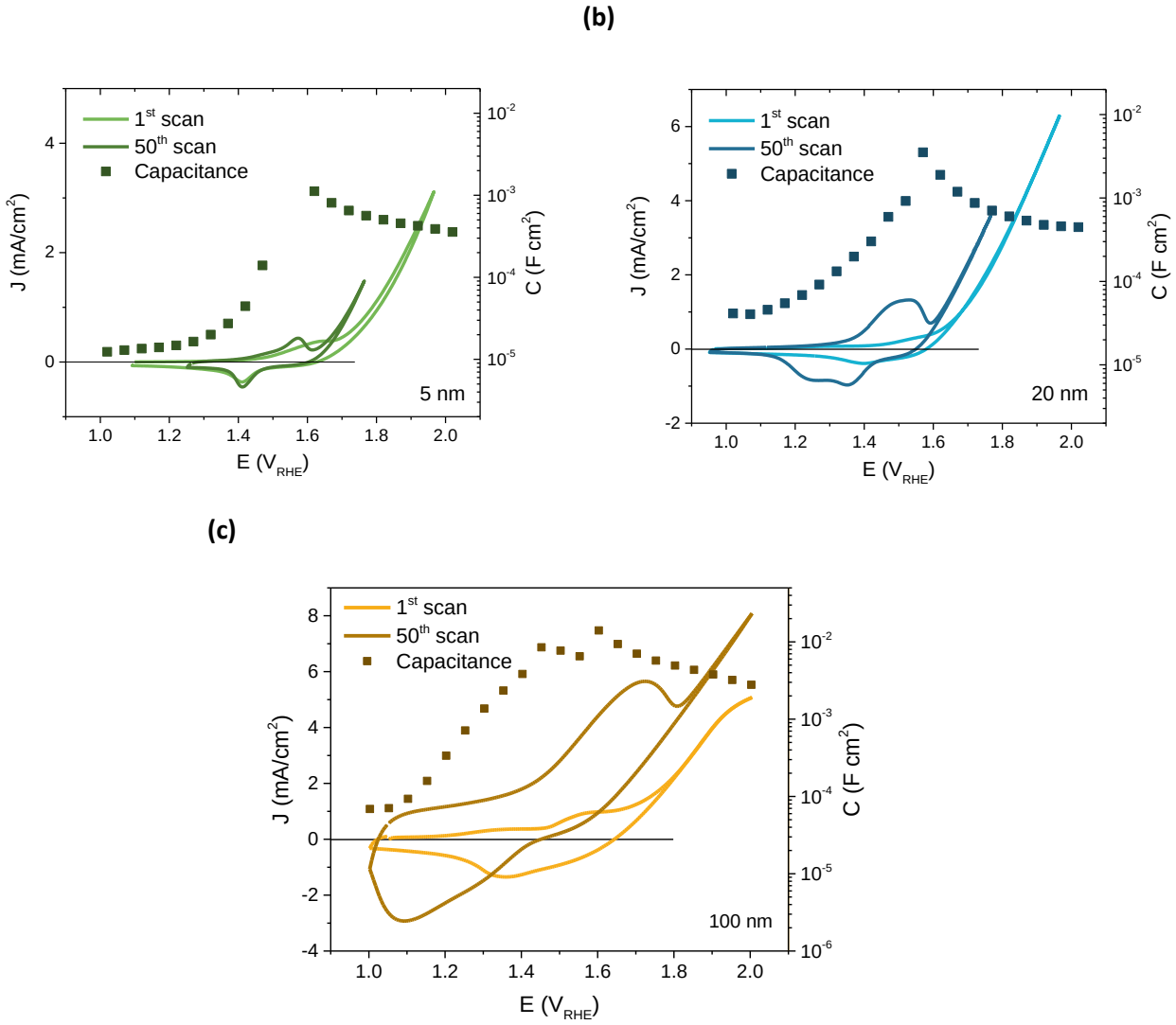

Figure S6. Cyclic voltamograms (lines) and calculated capacitance values (squares) of (a) 5 nm, (b) 20 nm and (c) 100 nm thick NiO_x films. Both the first CV scan (light colour) and 50th scan (dark colour) is given for each, as shown in Figure 1 for the 10 nm thick film. The scans were conducted at 50 mV/s in 0.1 M KOH pH=13.

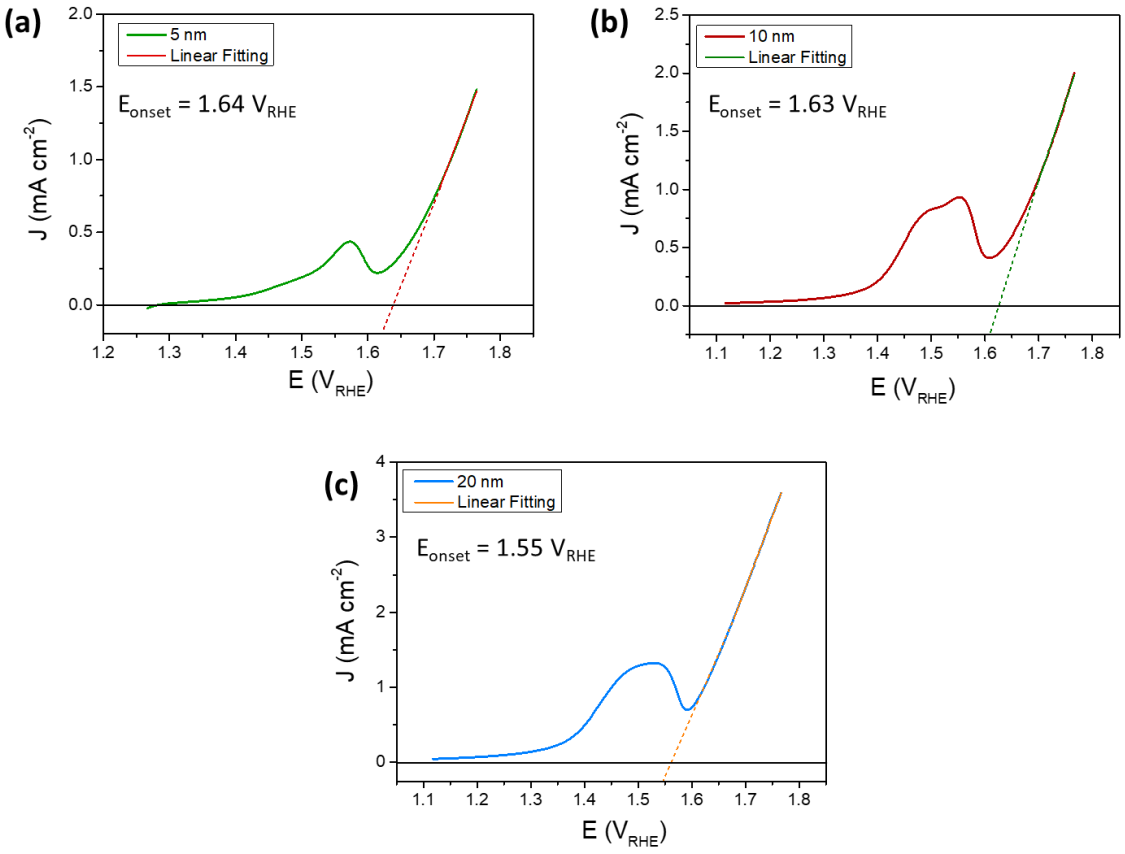

Figure S7. Determination of the onset potential as the potential where the linearly extrapolated catalytic current density reached 50 µA cm^{-2}, thereby minimizing the contribution of the redox wave. (a) 5nm, (b) 10 nm and (c) 20 nm samples. Exponential extrapolation at the same current density produces a similar result.

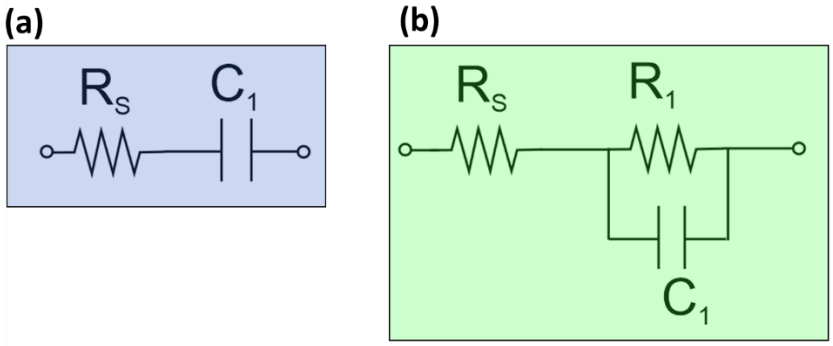

Figure S8. The equivalent circuit models used to fit the Nyquist plots to obtain capacitance values from electrochemical impedance data. Model (a) was used at low anodic potentials ($V<1.6\ V_{RHE}$) when the interface is blocked showing a pure capacitive behaviour, where model (b) was employed at high anodic potentials ($V>1.6\ V_{RHE}$) when charge transfer becomes measurable.

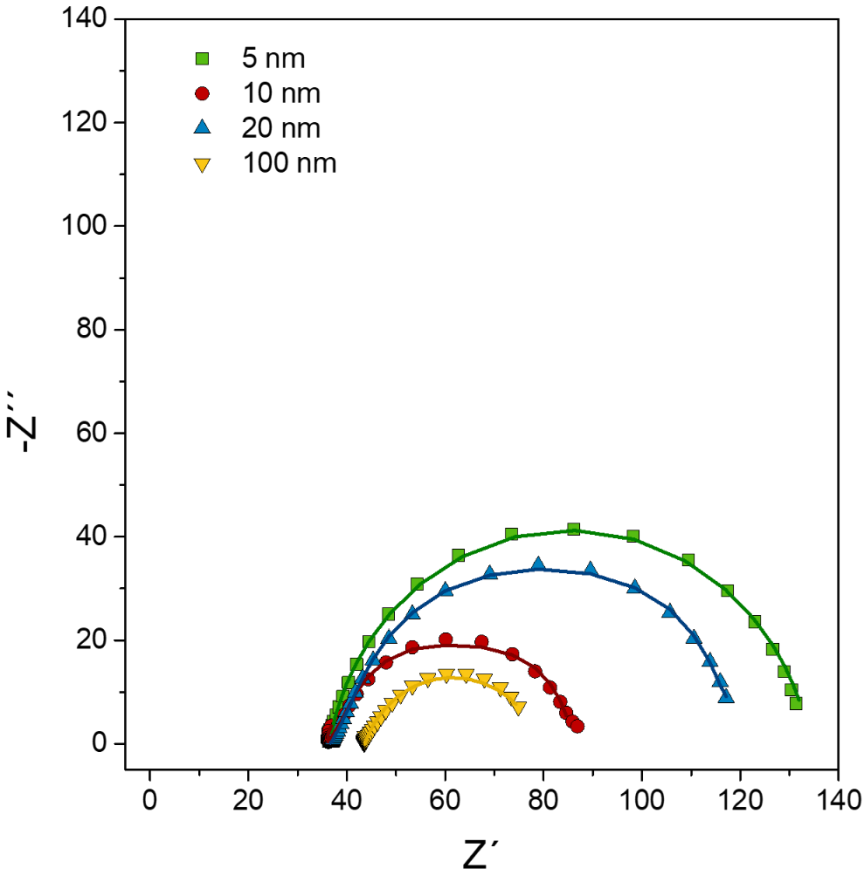

Figure S9. Nyquist plots for each thickness at 1.6 V_{RHE} showing the experimental points (symbols) and the fitting (continuous line).

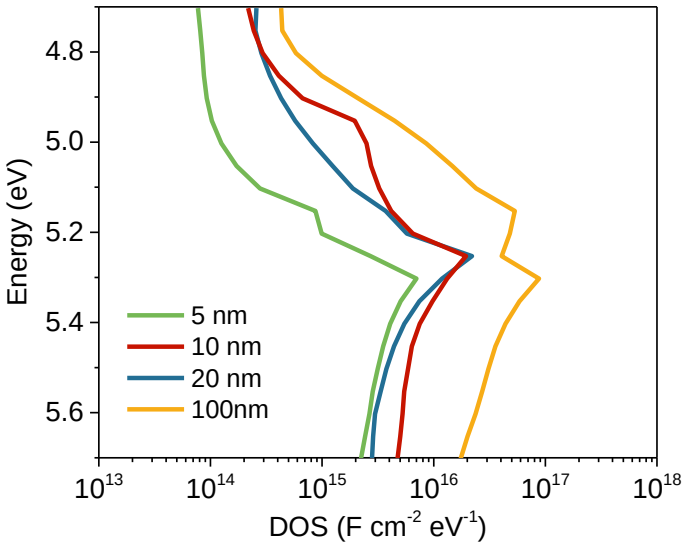

Figure S10. The Density of States (DOS) for each thickness, calculated from the chemical capacitance obtained from electrochemical impedance spectroscopy, using C = *e* x *DOS.*

As discussed in the main article, in the case of the 100 nm thick film, it is quite probable that not all of the film is activated from the 50 CV scans. This can be evidenced by SEC, which dominantly shows the spectrum of the NiOOH, rather than the species accumulated during catalysis (Figure S18). As such, this density of states is likely an underestimate of the true number of states generated in this pre-catalytic oxidation.

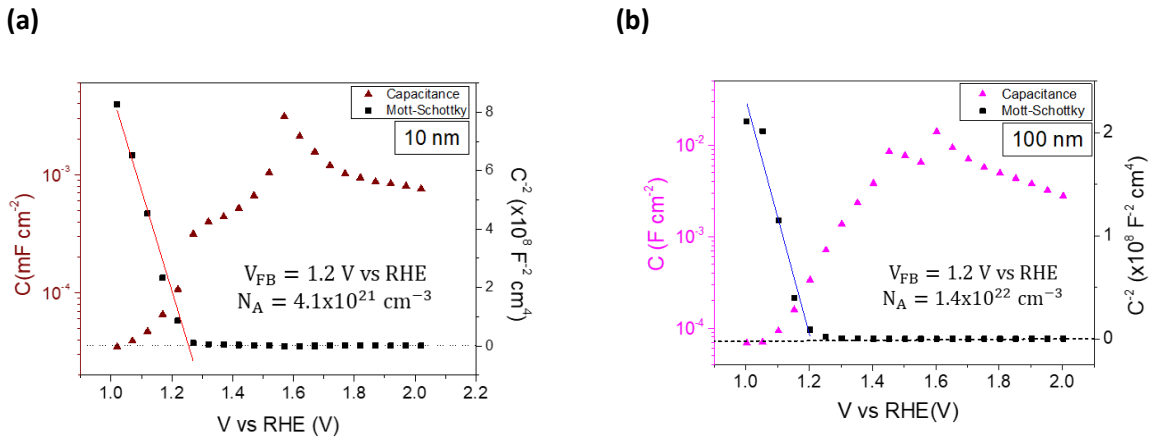

Figure S11. Mott-Schottky plots showing the p-type nature for samples of (a) 10nm and (b) 100 nm, affording calculation of a doping density around 10^{21} cm^{-3}. These two samples are representative of the analysed material.

Notice that the M-S analysis were carried out at the low anodic potential region ($V < 1.2\ V_{RHE}$), before the electrochemical transformation, where the sample is mainly NiOx, showing a semiconducting behaviour. The M-S analysis was carried out on the 10 and 100 nm samples. The depletion layer width was also calculated for these two samples (Figure S12).

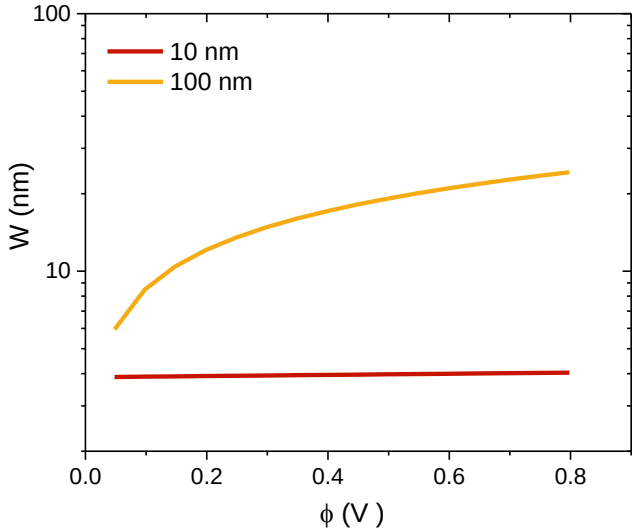

Figure S12. Depletion layer thickness calculated for samples of 10 nm and 100 nm. These two samples are representative of the analysed material.

G – Spectroelectrochemistry

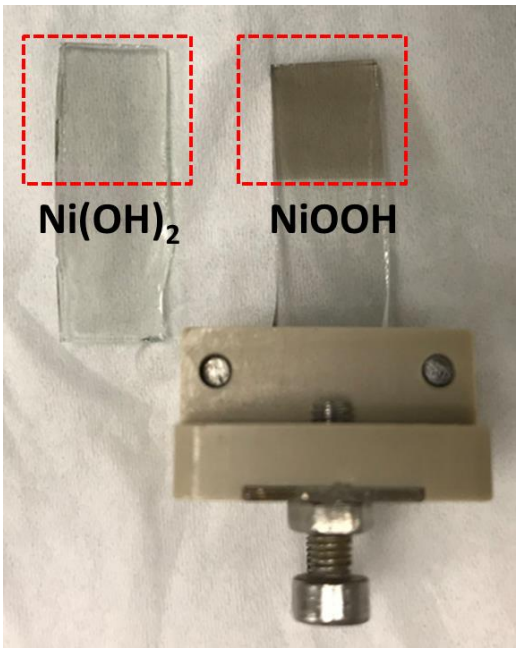

Figure S13. Photograph showing the change in opacity of the electrodes before (left) and after (right) activation, associated with the oxidation of Ni^{2+} to Ni^{3+}.

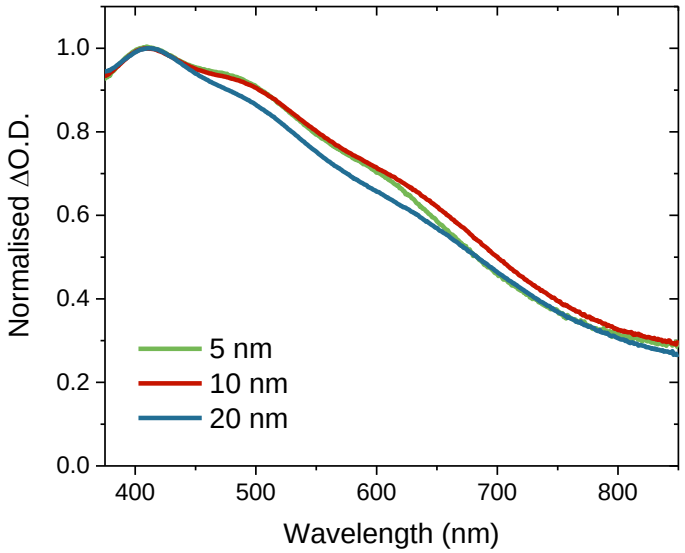

Figure S14. Normalised spectroelectrochemistry of each sample after activation, clearly demonstrating that the same species is formed at each thickness.

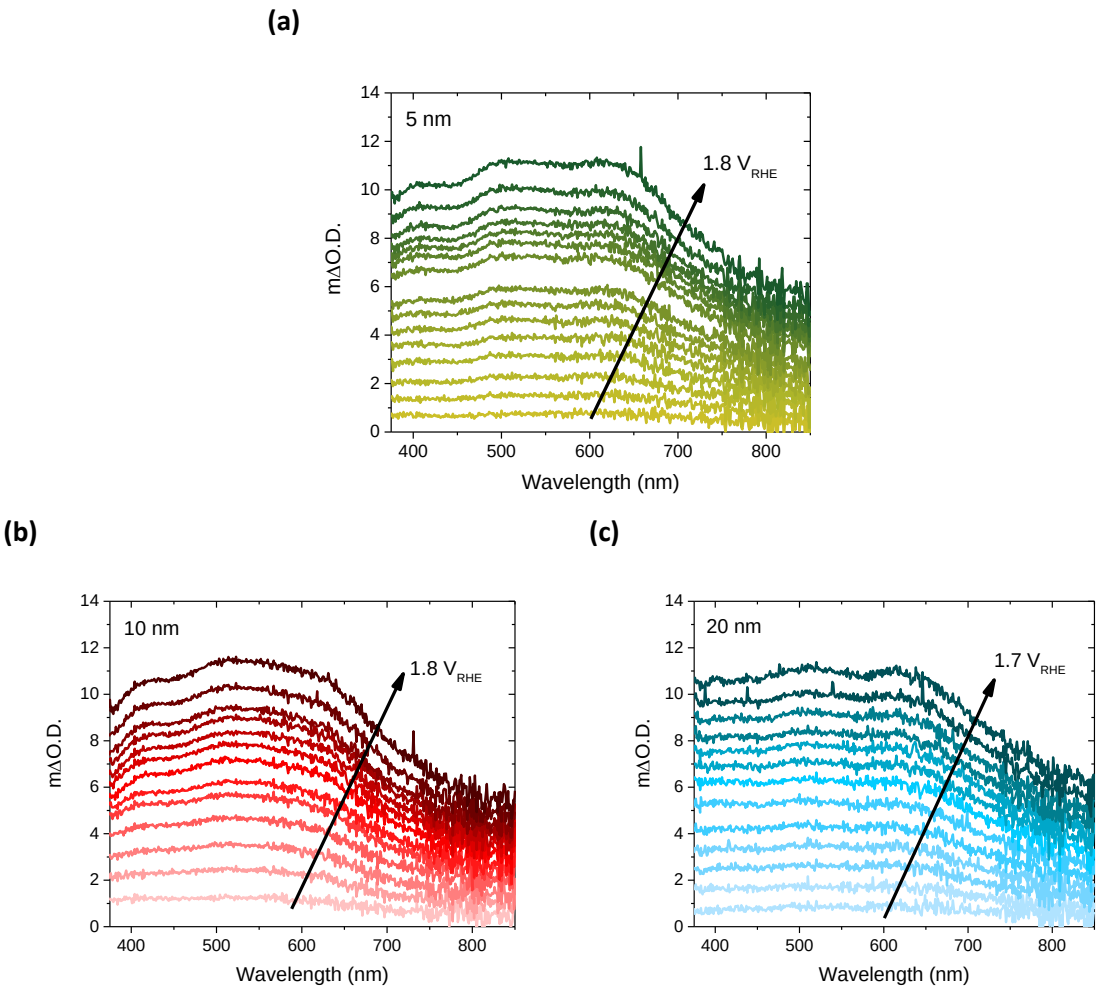

Figure S15. Spectroelectrochemistry over catalytic potentials with respect to the onset potential for (a) 5 nm, (b) 10 nm and (c) 20 nm films, as shown together in Figure 3a.

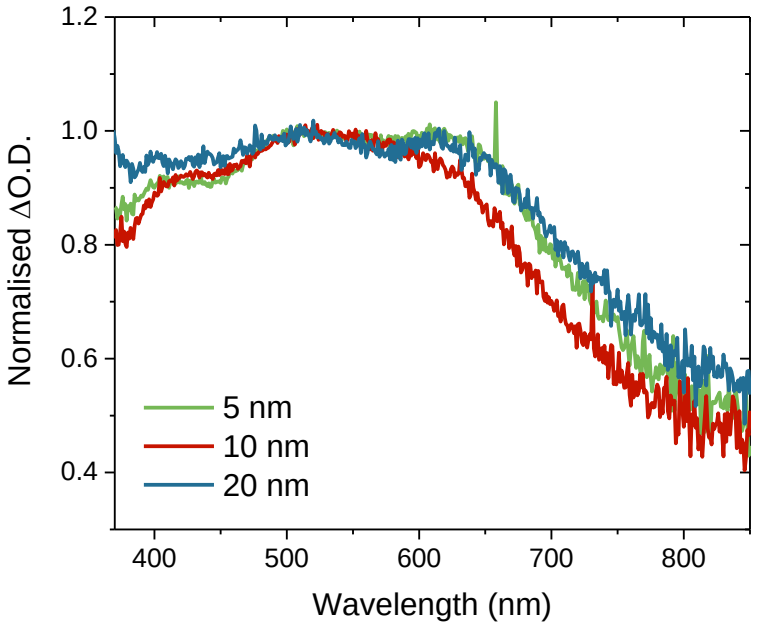

Figure S16. Normalised absorption spectra of the accumulated species over catalytic potentials for 5 nm (green), 10 nm (red) and 20 nm (blue) NiOOH films, 0.1 V after catalytic onset.

H – Indicators of incorporated Fe

Fe-incorporation has previously been shown to improve catalytic onset in metal oxyhydroxide structures, as well as increase current density, and the electrolyte used in this work was standard grade and not further purified 0.1M KOH, therefore likely to contain trace iron. Additionally, though the 20 nm NiOOH produces the same spectral features over catalytic potentials as the other films, the relative distribution of peaks is slightly broader and more blue-shifted (Figure S16), an observation previously reported in NiOOH films containing higher concentrations of Fe.[3-4]

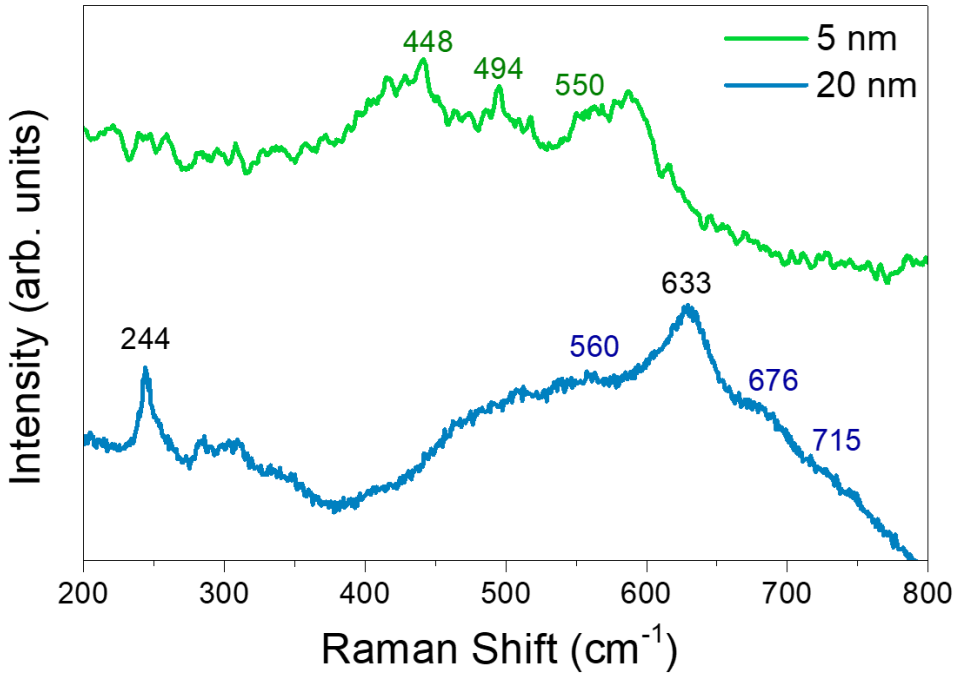

Figure S17. Normalised Raman spectra of the 5 nm (green) and 20 nm (blue) sample.

The Raman analysis of Figure S17 shows that the 5 nm sample presented two peaks around 448 and 494 cm^{-1} and a broad band around 550 cm^{-1}. The first peak is attributed to Ni-O vibrational modes present at both α-$Ni(OH)_2$ and β-$Ni(OH)_2$, which show peaks between 445-465 cm^{-1}.[5] The peak located at 494 cm^{-1} and the broad band at ~550 cm^{-1} are associated with a defective or disordered $Ni(OH)_2$ structure,[6-7] as anticipated from the deposition technique and in good agreement with other evidence in the manuscript, such as the high donor density extracted from Mott-Schottky analysis. These modes at 448 and 494 cm^{-1} are attenuated for the 20 nm sample, and the broad band is shifted to higher wavenumbers (~560 cm^{-1}), which may be attributed to higher Fe content, as reported previously.[8] Additionally, there are other contributions between 650-720 cm^{-1} in the 20 nm sample, which have been previously attributed to Fe phases.[8] The other two bands at 244 and 633 cm^{-1} are assigned to characteristic vibrational modes of FTO,[9] which is the underlying substrate of the active Ni-based electrocatalyst. However, an alternative explanation for the significant shift in Raman peaks in the 20 nm sample could be the presence of mixed NiOOH phases, also previously reported to shift the spectrum.[10] As such, either explanation could provide rationale for the improved performance of the thicker (20 nm) sample.

I – SEC of 100 nm sample

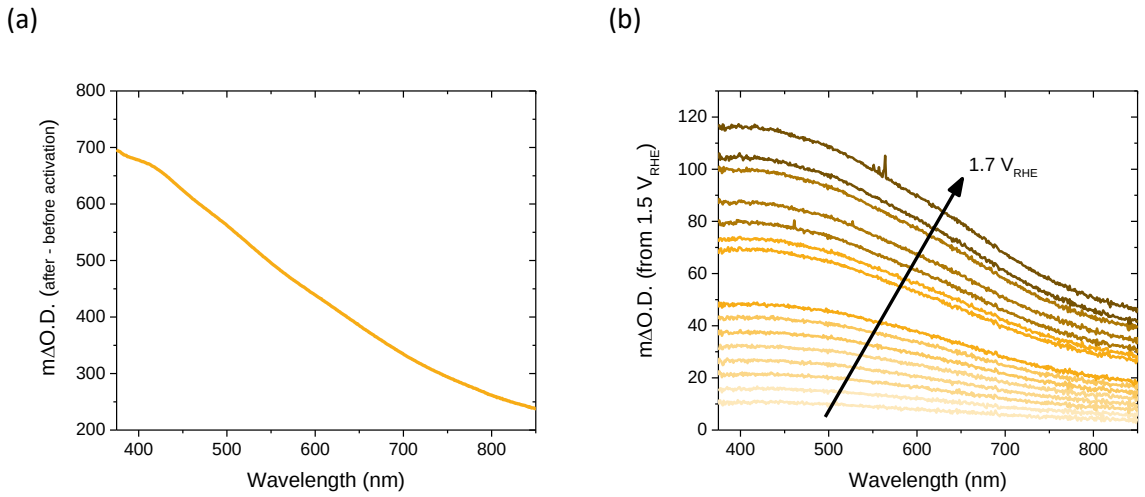

Figure S18. SEC of the 100 nm thick film showing the (a) pre-catalytic species and (b) the spectrum over catalytic potentials. It is evident from this data that the activation process (50 CV scans) is not adequate to oxidise the entirety of the film, and thus the spectrum at catalytic potentials is still dominated by absorption for NiOOH being generated.

J – References

1. Tengeler, S.; Kaiser, B.; Chaussende, D.; Jaegermann, W., (001) 3C SiC/Ni contact interface: In situ XPS observation of annealing induced Ni2Si formation and the resulting barrier height changes. *Applied Surface Science* **2017,** *400* (Supplement C), 6-13.
2. Rao, K. V.; Smakula, A., Dielectric Properties of Cobalt Oxide, Nickel Oxide, and Their Mixed Crystals. *Journal of Applied Physics* **1965,** *36* (6), 2031-2038.
3. Görlin, M.; Ferreira de Araújo, J.; Schmies, H.; Bernsmeier, D.; Dresp, S.; Gliech, M.; Jusys, Z.; Chernev, P.; Kraehnert, R.; Dau, H.; Strasser, P., Tracking Catalyst Redox States and Reaction Dynamics in Ni–Fe Oxyhydroxide Oxygen Evolution Reaction Electrocatalysts: The Role of Catalyst Support and Electrolyte pH. *Journal of the American Chemical Society* **2017,** *139* (5), 2070-2082.
4. Francàs, L.; Corby, S.; Selim, S.; Lee, D.; Mesa, C. A.; Godin, R.; Pastor, E.; Stephens, I. E. L.; Choi, K.-S.; Durrant, J. R., Spectroelectrochemical study of water oxidation on nickel and iron oxyhydroxide electrocatalysts. *Nature Communications* **2019,** *10* (1), 5208.
5. Kostecki, R.; McLarnon, F., Electrochemical and in situ raman spectroscopic characterization of nickel hydroxide electrodes I. pure nickel hydroxide. *Journal of The Electrochemical Society* **1997,** *144* (2), 485-493.
6. de Torresi, S. I. C.; Provazi, K.; Malta, M.; Torresi, R. M., Effect of Additives in the Stabilization of the α Phase of Ni (OH) 2 Electrodes. *Journal of The Electrochemical Society* **2001,** *148* (10), A1179-A1184.
7. Vidotti, M.; Salvador, R. P.; Ponzio, E. A.; Córdoba de Torresi, S. I., Mixed Ni/Co hydroxide nanoparticles synthesized by sonochemical method. *Journal of nanoscience and nanotechnology* **2007,** *7* (9), 3221-3226.
8. Louie, M. W.; Bell, A. T., An investigation of thin-film Ni–Fe oxide catalysts for the electrochemical evolution of oxygen. *Journal of the American Chemical Society* **2013,** *135* (33), 12329-12337.
9. Suresh, S.; Deepak, T. G.; Ni, C.; Sreekala, C. N. O.; Satyanarayana, M.; Nair, A. S.; Pillai, V. P. P. M., The role of crystallinity of the Nb2O5 blocking layer on the performance of dye-sensitized solar cells. *New Journal of Chemistry* **2016,** *40* (7), 6228-6237.
10. Yeo, B. S.; Bell, A. T., In situ Raman study of nickel oxide and gold-supported nickel oxide catalysts for the electrochemical evolution of oxygen. *The Journal of Physical Chemistry C* **2012,** *116* (15), 8394-8400.